Response of the Madden–Julian Oscillation and Tropical Atmosphere to Changes in Oceanic Mixed Layer Depth over the Indian Ocean

TERESA CICERONE,[a] TIMOTHY DELSOLE,[a] LAURIE TRENARY,[a] AND BEN KIRTMAN[b]

[a] *Department of Atmospheric, Oceanic, and Earth Sciences, George Mason University, Fairfax, Virginia*
[b] *Department of Atmospheric Sciences, Rosenstiel School for Marine and Atmospheric Science, University of Miami, Miami, Florida*

(Manuscript received 17 November 2021, in final form 1 February 2023, accepted 21 February 2023)

ABSTRACT: The Madden–Julian oscillation (MJO) is a component of tropical variability that influences high-impact events such as hurricane activity and Asian monsoons on intraseasonal (2–8 weeks) time scales. However, the atmosphere–ocean dynamics responsible for the MJO are highly debated. To gain insight into MJO–Indian Ocean dynamics, we conduct climate model experiments where the ocean is replaced by a motionless slab whose thickness, called the mixed layer depth (MLD), varies in space but not in time. Changes in the MLD and ocean heat convergence over the Indian Ocean have no discernible impact on MJO propagation, predictability, or variability within the Community Earth System Model (CESM) version 1.2.1. This suggests that ocean dynamics may not be critical to the MJO over the Indian Ocean in this dynamical model (CAM5 coupled to motionless slab). To diagnose changes in intraseasonal variability beyond the MJO, a discriminant analysis technique is used to optimize differences in variability between experiments. This analysis reveals that differences caused by changing Indian Ocean MLD were restricted mostly to local surface fluxes and could be explained by simple energy balance physics. Despite modeling adjustments intended to preserve the climate, the control slab has a warmer climate than the fully coupled model. The resulting changes in the mean climate are consistent with changes theoretically expected from global warming, particularly the "wet-gets-wetter" mechanism.

SIGNIFICANCE STATEMENT: The Madden–Julian oscillation (MJO) is a tropical eastward-moving pulse of convection that can influence a wide variety of global phenomena. Currently, models do not capture many key aspects of the MJO such as speed and spatial structure. The uppermost ocean layer that communicates with the atmosphere is widely believed to play a large role in the evolution of the MJO. To test the importance of ocean dynamics on simulated MJO, a slab-model configuration is used to allow the atmosphere and ocean to communicate through surface fluxes of heat and moisture while suppressing interactive ocean currents. Changes to the upper ocean did not impact the MJO in our model setup.

KEYWORDS: Madden-Julian oscillation; Oceanic mixed layer; Statistical techniques; Statistics

1. Introduction

While analyzing surface pressure and zonal wind data from Canton Island, Roland Madden and Paul Julian stumbled upon a mode of tropical variation in the form of a large zonal circulation cell (Madden and Julian 1971). Madden and Julian later extended their research by adding other stations across the tropics. They found a clear eastward-moving signal that started in the Indian Ocean and moved into the Pacific (Madden and Julian 1972). This component of variability is now called the Madden–Julian oscillation (MJO) and is the dominant mode of tropical intraseasonal variability on 30–60-day time scales. Since its discovery in 1971, the MJO has been found to have significant global impacts (Zhang 2013; Lau and Waliser 2012). The MJO sits in the gap between weather and climate and affects several phenomena across both temporal scales from hurricanes in the Gulf of Mexico to the monsoons in India (Klotzbach 2010; Taraphdar et al. 2018; Goswami et al. 2003). The MJO has direct and indirect impacts on the world's most populous countries, making understanding, modeling, and predicting the MJO of high socioeconomic importance (Wang 2006).

Models often fail to simulate basic features of the MJO, including the eastward propagation speed, spatial structure, and variance (e.g., Kim et al. 2009; Hung et al. 2013; Jiang et al. 2015; Ahn et al. 2017; Lin et al. 2006). Jiang et al. (2015) found that out of twenty-seven 20-yr climate simulation models from different institutions, only 25% were able to simulate a realistic eastward propagation. Hung et al. (2013) found that only 1 out of 20 CMIP5 models is able to do so. CMIP6 models show an improvement to simulated MJO propagation (Ahn et al. 2020). However, even when a model is able to produce a realistic eastward propagation, the speed is often too fast (Kim et al. 2009; Ahn et al. 2017) or the variance is not strong enough (Lin et al. 2006). Even if a model produces a better representation of an MJO event, the fundamental physics behind the improved simulation is not well understood (Jiang et al. 2020).

Numerous studies suggest that the inability of climate models to simulate a realistic MJO may in part be due to deficiencies in modeling the dynamics of oceanic mixed layer (e.g., DeMott et al. 2015; Ling et al. 2017; Anber et al. 2017; Maloney and Sobel 2004). In particular, climate models have difficulty in simulating a realistic mixed layer depth (MLD). Overly deep mixed layers are a common bias in most climate models (e.g., de Boyer Montégut et al. 2004; Huang et al. 2014). Further, tropical precipitation amplitude and propagation, ocean heat content, and sea surface

Corresponding author: Teresa Cicerone, tciceron@gmu.edu

DOI: 10.1175/JCLI-D-21-0788.1

© 2023 American Meteorological Society. For information regarding reuse of this content and general copyright information, consult the AMS Copyright Policy (www.ametsoc.org/PUBSReuseLicenses).

Brought to you by NOAA Central Library | Unauthenticated | Downloaded 01/16/24 09:04 PM UTC

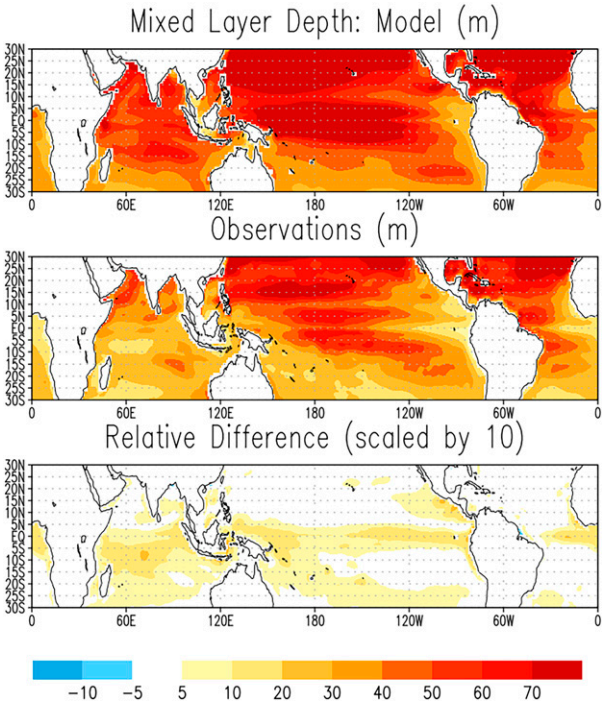

FIG. 1. Mixed layer depth (MLD; m) in (top) the fully coupled CCSM4 model, (middle) the observational GODAS, and (bottom) the difference (CCSM4 − GODAS) divided by GODAS MLD × 10. All values averaged over the years 1982–2000.

temperatures (SSTs) on intraseasonal time scales are strongly affected by the structure of the upper ocean.

To take a specific example, we show in Figs. 1a and 1b the average MLD for observations and CCSM4 forecasts [the CCSM4 forecasts are from the North American Multimodel Experiment, as discussed in Kirtman et al. (2014)]. As can be seen in the Fig. 1, the modeled layer depth is nearly twice as deep as corresponding observations, with the biggest fractional error occurring in the Indian Ocean. These differences are shown in Fig. 1c. Notably, the greatest discrepancy appear to be associated with the Seychelles–Chagos Thermocline Ridge (SCTR), an open ocean upwelling zone in southern Indian Ocean that can limit the depth of the mixed layer to less than 10 m (Trenary and Han 2012; Hermes and Reason 2008; McCreary et al. 1993; Woodberry et al. 1989; Vialard et al. 2009). The shallowness of the mixed layer in the SCTR region has been shown to significantly impact surface fluxes of heat and moisture (Duvel et al. 2004; Ling et al. 2017). Moist processes have been shown to have a large impact on MJO structure and development (e.g., Jiang et al. 2018; DeMott et al. 2019; Flatau et al. 1997), and are at the center of most MJO dynamics theories (Jiang et al. 2020). Likewise, thermodynamic ocean processes interacting with the atmosphere have been shown to produce key MJO characteristics, such as propagation speed and periodicity (e.g., Wang and Xie 1998). Satellite data and reanalysis confirm a coherent relationship between precipitation, SST, and surface fluxes during an MJO event (Woolnough et al. 2000). Namely, the MJO drives oceanic changes through heat fluxes (shortwave and longwave radiation, sensible and latent heat fluxes), precipitation, and surface wind stress (Woolnough et al. 2000). Preceding MJO convection there is an increase in incoming shortwave radiation producing warm SST anomalies, a decrease in latent heat flux, and a decrease in surface winds. During convection there is a reduction in shortwave radiation due to cloud cover, and SST cooling due to increased evaporation from westerly wind bursts. The ocean responds with MJO induced SSTs anomalies and upper-ocean changes that can modulate or directly induce atmosphere–ocean heat exchange (e.g., Drushka et al. 2012; Shinoda et al. 2017; Masumoto and Meyers 1998; Xie et al. 2002; Hermes and Reason 2009; DeMott et al. 2015) that have been shown to produce MJO events (e.g., Bulusu 2016; DeMott et al. 2015).

Further, it is believed that the strong air–sea coupling in the SCTR may impact the development and evolution of the MJO (Vialard et al. 2009, 2008). While there has been considerable focus on the effects of atmosphere–ocean dynamics on the MJO within the SCTR, there remains relatively little known about the role of atmosphere–ocean dynamics across the tropical Indian Ocean in determining MJO characteristics, such as convective strength, eastward propagation, predictability, and variability (Wang et al. 2012; Ray and Zhang 2010; DeMott et al. 2015; Shoup et al. 2020; Phillips et al. 2021; Hagos et al. 2020). Thus, this paper explores the sensitivity of tropical variability to MLD changes over the Indian Ocean (25°N–20°S and 40°–100°E).

Using historical data from a single CESM large-ensemble simulation and CESM version 1.2.1, we perform a series of experiments designed to clarify the dependence between oceanic MLD and MJO and more broadly the tropical circulation, including its mean structure and intraseasonal variability. Specifically, we start with CESM's in its fully coupled configuration and replace CESMs dynamical ocean model with a motionless slab. From there, we adjust the MLD in the slab in various ways, particularly over the Indian Ocean. We then study the resulting changes in the tropical circulation to gain insight into the role of the MLD in tropical circulation.

2. Data

a. *Climate model*

CESM1.2.1 uses Community Atmosphere Model version 5 (CAM5), Parallel Ocean Program (POP) version 2 from Los Alamos National Laboratory (LANL), and the Community Land Model version 4 (CLM4) with Carbon Nitrogen (CN) (Hurrell et al. 2013). We use the default physics package for CAM5 with a finite volume dynamical core on 1.9° × 2.50° latitude × longitude grid with thirty vertical levels.

CAM5 parameterizes deep convection using the Zhang and McFarlane (1995) convective scheme. This convective parameterization scheme has three core components (trigger function, closure assumption, and bulk cloud model) with a convective available potential energy (CAPE)-based closure. The trigger function determines the occurrence of convection and "triggers" the convective scheme when the CAPE is

Brought to you by NOAA Central Library | Unauthenticated | Downloaded 01/16/24 09:04 PM UTC

greater than 70 J kg^{-1}. The closure assumption determines the convective intensity (includes effects from large-scale forcing) and assumes that the convection acts to consume the CAPE. Finally, the bulk cloud model determines convective transport and the vertical distribution of convective heating and drying (Song and Zhang 2018; Conley 2012). Specifically, the moist turbulence scheme from Bretherton et al. (2004), is responsible for the vertical transport of heat and communicates with the surface heat flux scheme (functions of SST) (Conley 2012). CAM obeys the fundamental balances of energy, momentum, and moisture.

It is important to note that climatologies (mean states) within the model are vital to MJO simulations (e.g., Inness and Slingo 2003). The model needs to be able to reproduce basic features such as intertropical convergence zone location, westerly lower tropospheric winds, and mean SST distribution. The climatologies will be discussed in detail in section 3a, but both the fully coupled and slab control run are able to produce the basic features vital to the MJO simulations. However, CAM5 alone struggles to capture key features of an MJO event including spatiotemporal variability (e.g., Lan et al. 2022; Jiang et al. 2015; Boyle et al. 2015). One hypothesis for the poor MJO simulation is that the coupled model has an excessively deep ML in the Indian Ocean, which affects the air–sea interaction. To explore this hypothesis, we conduct sensitivity experiments to see if removing this bias changes (and hopefully improves) the MJO simulations.

b. Coupled and control model runs

In this study, all data are interpolated to a 1.9° × 2.50° grid, with a daily coupling rate between atmosphere and ocean models. To focus our efforts on the tropics, we restrict our analysis of tropical variability to 30°S–30°N. Our first dataset is a fully coupled run which uses the CESM large-ensemble simulation with 1850–2000 transient forcing (output data made using CCSM4). More information on the CESM large-ensemble project can be found in Kay et al. (2015). The fully coupled run is evaluated over the years 1850–70. Bui and Maloney (2019) found barely detectable MJO changes even after 100 years of forcing, therefore we conclude that there are no differences in MJO from the CESM transient forcing and preindustrial control simulations. This was further confirmed by comparing auto- and cross correlations between the fully coupled model from 1850 to 1870 and from 1980 to 2005, where we found no statistical difference between the two time periods.

Note here that the fully coupled model data differ from what was presented in Fig. 1. Both are from CCSM4, but Fig. 1 MLD spans the years 1982–2000, while the fully coupled simulation spans 1850–70. Figure 1 was chosen to match observational data, and the fully coupled data were chosen to match our experiments.

For our control run, we replace the dynamical ocean model with a motionless slab, or slab ocean model (SOM). The SOM represents a well-mixed ocean mixed layer with no horizontal communication between ocean columns, while allowing for interaction with the overlying atmosphere through heat and moisture fluxes. Thus, a SOM removes interactive ocean dynamics but keeps thermodynamic coupling.

The SOM equation is derived from the heat content of an ocean layer (Q_h) defined as

$$Q_h = \rho c_p T h, \tag{1}$$

where ρ and c_p are the density and specific heat of seawater, respectively; T is ocean temperature; and h is the mixed layer depth. Conservation of energy leads to the standard SOM equation,

$$\rho c_p h \frac{dT}{dt} = q_o - Q_{dp}, \tag{2}$$

where q_o is the net surface energy flux (net shortwave radiation minus the sum of surface longwave radiation, and latent/sensible heat fluxes) and dt is 2 months. The "q flux" term (i.e., ocean heat flux convergence Q_{dp}) accounts for entrainment/detrainment at the bottom boundary and for horizontal heat transport not included in a SOM. The Q_{dp} is computed as a residual from Eq. (2) where SSTs, MLD (h), and q_o are annual averages from the fully coupled run [see Bitz et al. (2012) for more information].

The Q_{dp} is derived to maintain the SSTs found in the fully coupled run, alleviating concern that the SOM will produce a climate that differs from the fully coupled simulation. The prognostic variable of mixed layer temperature (T) is calculated by integrating Eq. (2) over time. Using Eq. (2) allows for the fully interactive treatment of thermodynamic exchange of energy between the atmosphere and ocean surface.

c. Mixed layer depth experiment model runs

Due to model biases, the MLD in the coupled model (and therefore the SOM control run) is generally deeper than in observations, particularly over the thermocline ridge in the Indian Ocean (SCTR). Therefore, we want to run a set of experiments where we shoal the MLD over the Indian Ocean. These experiments are similar to those used in previous studies (e.g., Maloney and Sobel 2004; Maloney and Kiehl 2002; Marshall et al. 2008). In one experiment we fix the MLD in the Indian Ocean (25°N–20°S and 40°–100°E) to 2 m without changing Q_{dp} (function of surface temperature and MLD). We call this run, "2mIO." In another experiment, we fix the MLD in the Indian Ocean to 2 m and adjust Q_{dp} to maintain the climatology of the fully coupled model. We call this run "2mIOqadj." This unadjusted run allows the climatology to drift, but this may be easier to interpret because only one change was made to the model. Additionally, we ran five other runs similar to 2mIO accept the MLD was set to 10, 20, 30, 40, and 50 m to test MLD sensitivity over more realistic values. Each experiment is run over a period of 20 years, initiated in 1850. All experiments are listed in Table 1. Note that for the sensitivity experiments, changes are only made to the Indian Ocean. MLD and Q_{dp} values outside of the Indian Ocean are always set to spatially varying annually averaged fully coupled values (i.e., control run values, see Fig. A1 in the appendix).

Brought to you by NOAA Central Library | Unauthenticated | Downloaded 01/16/24 09:04 PM UTC

TABLE 1. Experiment list.

Experiment name	Indian Ocean MLD value (m)	Indian Ocean Q_{dp} value	Average MLD change from control run value (m)
Fully Coupled	Interactive	N/A uses POP	—
Control	Spatially varying	Spatially varying	—
2mIO	2	Spatially varying	30 decrease
2mIOqadj	2	Function of MLD [see Eq. (2)]	30 decrease
10mIO	10	Spatially varying	22 decrease
20mIO	20	Spatially varying	12 decrease
30mIO	30	Spatially varying	2 decrease
40mIO	40	Spatially varying	7 increase
50mIO	50	Spatially varying	17 increase

d. *Observational data*

For comparison with observations, we use the National Oceanic and Atmospheric Administration (NOAA) interpolated outgoing longwave radiation (olr) (Liebmann and Smith 1996) and the National Centers for Environmental Prediction–National Center for Atmospheric Research (NCEP–NCAR) Reanalysis 1 for the zonal winds (Kalnay et al. 1996; NCEP et al. 1994). All observational data are interpolated to a 1.9° latitude × 2.50° longitude grid and evaluated over the years 1979–2016.

3. Changes in the mean and in the MJO

a. *Diagnosing changes in mean state climatology*

Despite including Q_{dp} to preserve the climate, the SOM control run has a warmer climate than the fully coupled run (see Fig. 2). This is because the derivation of Q_{dp} effectively assumes that the surface fluxes in the two models are the same on average, which is not the case because coupled atmosphere ocean interactions differ between the SOM and dynamical ocean configurations. Because the control run ends up being somewhat warmer than the fully coupled run, we expect the corresponding changes in other climate variables to be consistent with changes predicted under global warming, for instance the "wet-gets-wetter" mechanism of Held and Soden (2006).

To test this expectation, Fig. 3 shows a comparison of the climatological precipitation in the fully coupled run, and the change in precipitation between the fully coupled and SOM control run. Much of the increase in the change in precipitation occurs over the wettest regions, consistent with the wet-gets-wetter mechanism, but the patterns are not exact, particularly over the coasts. Other changes in the mean can be predicted based on known relations with precipitation. For instance, increasing precipitation in the control run corresponds to increased convection, decreased net surface shortwave radiation, increased net surface longwave radiation, and decreased outgoing longwave radiation (not shown). Note that the double ITCZ, or the addition of excessive precipitation in the Southern Hemisphere, is a common model problem (Hwang and Frierson 2013). In the present study, this model error is not critical because our goal is to understand the impact of *changes* in ocean model within a physically consistent dynamical system.

b. *Quantifying the MJO*

To evaluate differences in the MJO between the model runs and observations, we use the revised real-time multivariate MJO (RMMr) index (see Wheeler and Hendon 2004; Liu et al. 2016). The propagation, predictability, and variability of the MJO can be assessed from the RMM1 and RMM2 indices making it widely used in MJO studies (Dasgupta et al. 2020). For example, predictability is measured from the decay of the autocorrelation function time of RMM1 and RMM2, variability is measured by variance, and propagation is measured by cross correlations. Our daily data are projected onto the empirical orthogonal function (EOF) patterns of Wheeler and Hendon (2004) (i.e., observations). We examined composites between MJO and other variables in the model, but it is difficult to know if the differences are significant just by eye. A more rigorous statistical approach is to compare auto- and cross correlations between the RMMr1 and RMMr2 time series. Autocorrelations can be used to characterize memory/persistence and cross correlations can be used to characterize

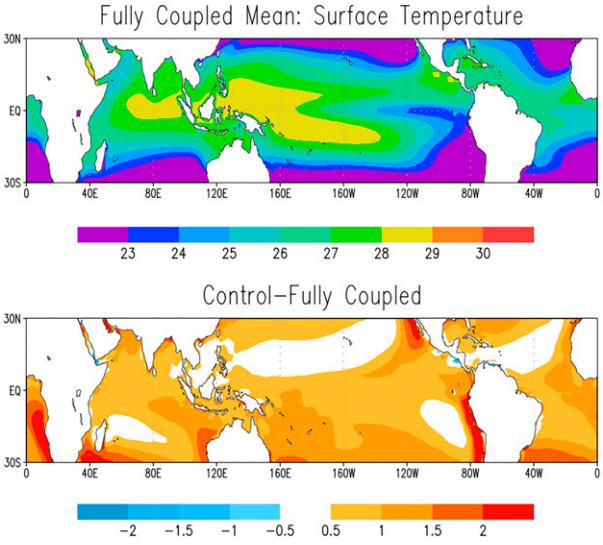

FIG. 2. (top) The mean surface temperature (°C) in the fully coupled run and (bottom) the difference in mean surface temperature (°C) for the control slab minus fully coupled runs.

Brought to you by NOAA Central Library | Unauthenticated | Downloaded 01/16/24 09:04 PM UTC

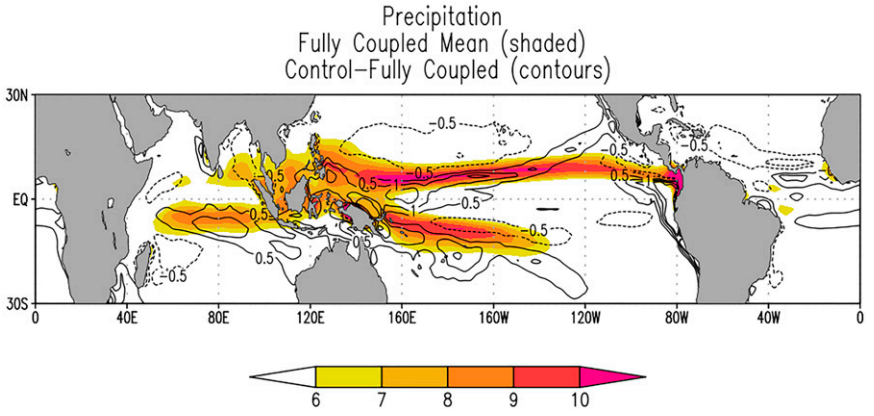

FIG. 3. Mean precipitation (mm day^{-1}) for the fully coupled run (shading) and the difference between the control slab and fully coupled runs (contouring).

propagation. We also examined other MJO metrics including Hovmöller plots, wavenumber–frequency spectra, and regression patterns (e.g., Waliser et al. 2009; Wang et al. 2015). These alternative metrics consistently indicated that the MJO did not change significantly, which is not surprising since each of these metrics are derived from the RMM1 and RMM2 indices, which themselves show few differences. However, a rigorous significance test for differences in these alternative metrics is lacking, therefore results from these metrics will not be discussed further.

However, it was hard to make a definitive decision if the MJO changed significantly since these figures were evaluated by eye. Once we discovered that active ocean dynamics did not improve the models' simulation of the MJO from the auto-/cross correlations, we decided not to delve into processes and excluded other MJO diagnostics.

To account for serial correlation, the RMMr 20-yr time series are split into two 10-yr periods and the correlations are computed separately for each 10-yr period. When the difference within the same experiment is comparable to the

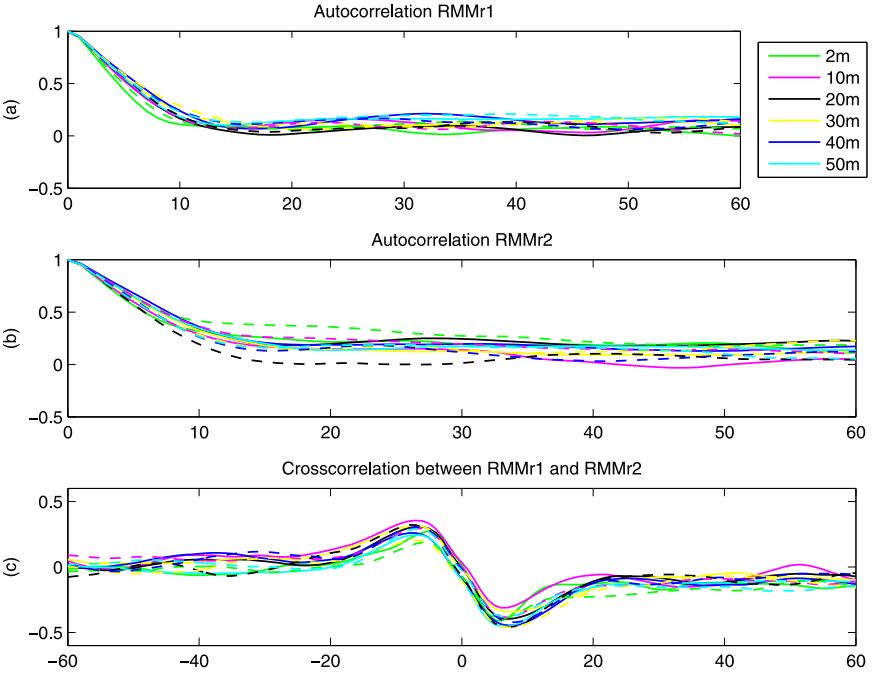

FIG. 4. Autocorrelation as a function of lag (in days) for all Indian Ocean MLD values in SOM experiments (see Table 1). (a) Autocorrelations for RMMr1, (b) autocorrelations for RMMr2, and (c) cross correlations between RMMr1 and RMMr2. Solid and dashed lines of the same color denote the first and second half of the same time series.

Brought to you by NOAA Central Library | Unauthenticated | Downloaded 01/16/24 09:04 PM UTC

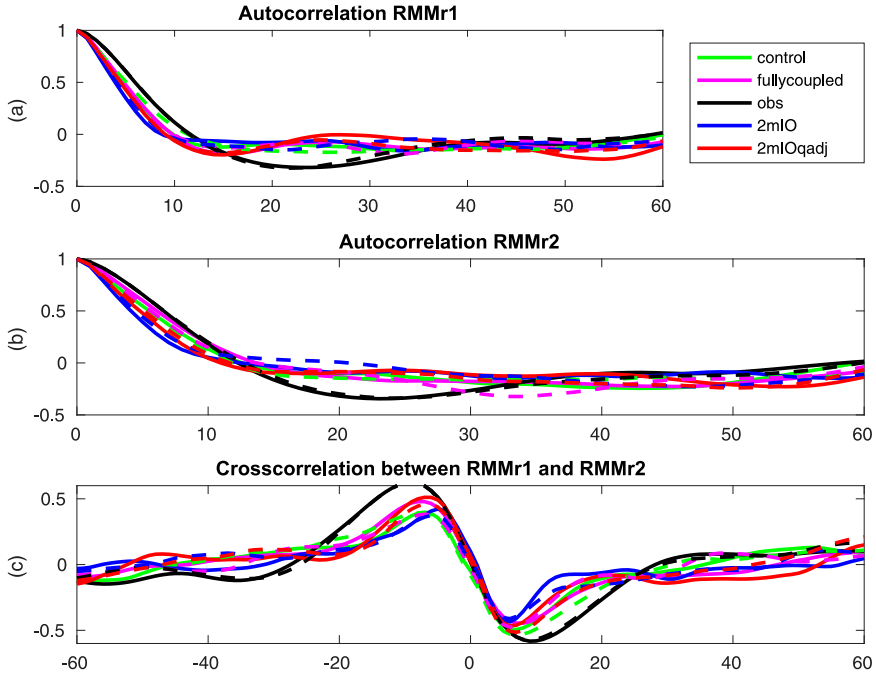

FIG. 5. As in Fig. 4, but adding the auto- and cross correlations for the 2-m MLD sensitivity experiments.

difference between experiments, we can conclude that there is no significant change in variability between experiments. Preliminary analysis of auto- and cross correlations in our experiments showed no difference between seasons (i.e., boreal winter versus summer), so we reported the full time series in our analysis.

The autocorrelation function for RMMr1 and RMMr2 and the cross-correlation function between RMMr1 and RMMr2 are shown in Fig. 4 for all Indian Ocean MLD change experiments listed in Table 1. Results from different model experiments are shown in different colors and the corresponding dashed and the solid curves show the estimates from two 10-yr periods between the same experiment. Comparing the auto- and cross correlations across model experiments, we see that at lags less than 10 days there is little difference in autocorrelations between experiments. At longer lag times, the two estimates from the same experiment diverge, illustrating an increase in sampling error. As a result, we conclude there is not a significant MJO difference between subdivided 10-yr data segments. Due to this finding of no MJO sensitivity among MLD values, including at more realistic values between 15 and 30 m (e.g., Maloney and Sobel 2004), we will now only report the extreme case of an MLD shoaled to 2 m.

Similar to Fig. 4, Fig. 5 shows the autocorrelation function for RMMr1 and RMMr2 and the cross-correlation function between RMMr1 and RMMr2 but now comparing the 2 m SOM cases (2mIO and 2mIOqadj) with the SOM control, fully coupled run, and observations. Again, we see there is little difference in autocorrelations between experiments at lags less than 10 days, implying that changing the MLD, in this case reducing the SOM thickness to 2 m (over the Indian Ocean), and ocean model (e.g., fully coupled to SOM) have little impact on MJO variability. We also see that the observed RMMr index shows stronger oscillations compared to the model RMMr, which tend to decay to zero with little oscillatory behaviors further indicating the model does not produce a realistic MJO.

c. *Isolating impacts on climate variability*

We now want to consider changes in intraseasonal variability. To do this, we remove the 120-day running mean from the data, following the methodology used in RMM index calculations (e.g., Wheeler and Hendon 2004; Liu et al. 2016; Gottschalck et al. 2010; Martin et al. 2020) to isolate intraseasonal variability and remove interannual variability, decadal variability, and trends. Further, averaging over 15°S and 15°N smooths out the majority of tropical synoptic scale waves (Wheeler and Hendon 2004; Liu et al. 2016). We then assume that the mean (μ) and variance (σ^2) of precipitation follow the power law:

$$\sigma^2 = k\mu^{\alpha}, \tag{3}$$

where α is the power-law exponent and k is a constant. We make this assumption because power laws describe phenomena that "cluster" at one end of a distribution (e.g., precipitation, where extreme events are infrequent) (Olsson and Burlando 2002; Cavanaugh et al. 2015). This is similar to the work done by Shin et al. (2016), who use the power law to relate rainfall kinetic energy to rainfall intensity. Small changes in (3) are governed by the differential,

$$d\log\sigma^2 = \alpha d\log\mu. \tag{4}$$

Brought to you by NOAA Central Library | Unauthenticated | Downloaded 01/16/24 09:04 PM UTC

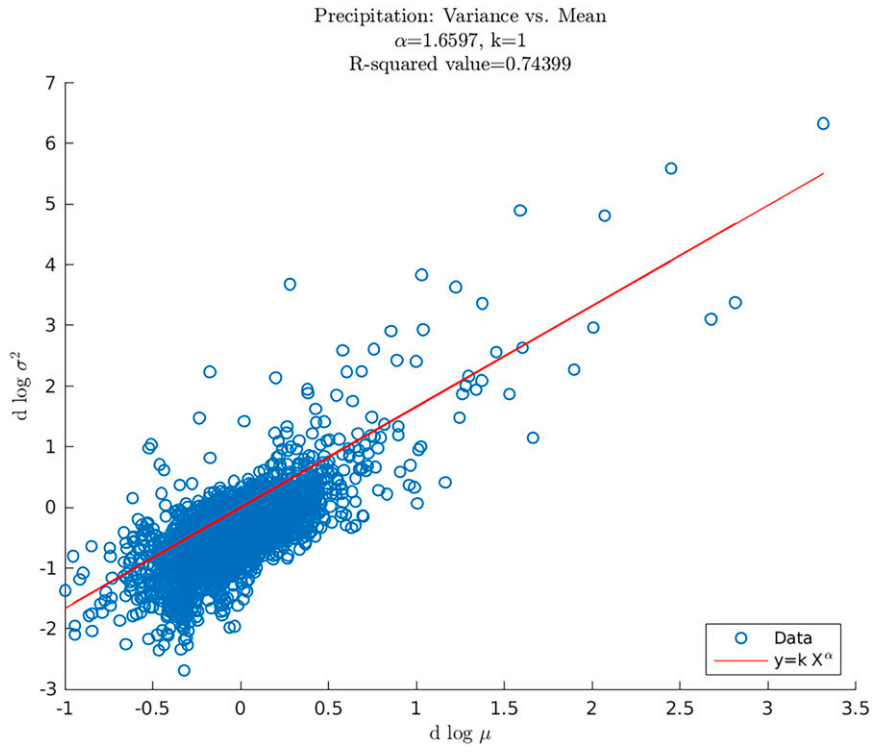

FIG. 6. Scatterplot of $d\log\sigma^2$ vs $d\log\mu$ for precipitation (mm day^{-1}) where σ^2 and μ refer to the variance and mean, respectively. The corresponding power law fit is shown in red.

Figure 6 shows a scatter diagram of $d\log\sigma^2$ versus $d\log\mu$. The line fit to these data gives an estimate of α as 1.7 with the intercept fixed to 0. Integrating the differential in Eq. (4) gives

$$\frac{\sigma^2_{\text{control}}}{\sigma^2_{\text{fullycoupled}}} = \left(\frac{\mu_{\text{control}}}{\mu_{\text{fullycoupled}}}\right)^{\alpha}. \tag{5}$$

The predicted change in the ratio of variance for precipitation estimated from Eq. (5) is shown in Fig. 7. Comparing to the corresponding actual (i.e., point-by-point or local) variance ratio shows that, while there are some differences, the above model is able to produce the gross structure and amplitude of the mean precipitation ratio. Up to this point, our analysis indicates that intraseasonal variability of precipitation differs between model experiments. However, for this analysis to be meaningful, we must determine if the changes in variability of the individual climate variables are statistically significant.

4. Did the variability change outside of the MJO?

In this section, we discuss a statistical optimization procedure called covariant discriminant analysis (CDA), which will be used to establish the field significance of changes in variance. Note that while simpler significance test methods exist (e.g., *F* test and variance differences), those methods are only local and do not rule out changes in modes of variability. In contrast, CDA is able to identify changes in modes of variability.

a. *Covariant discriminant analysis*

To test the significance of changes in variability, we want to compare variability between our experiments. EOFs are a standard way of characterizing variability, but EOFs are not the best way to *compare* variability. For instance, the biggest

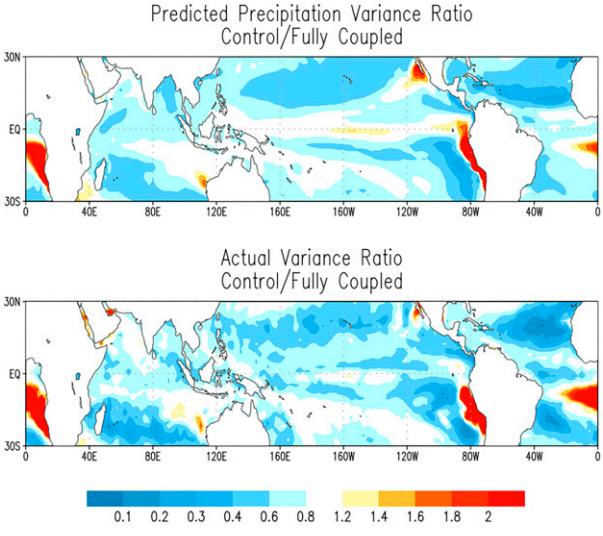

FIG. 7. (top) Predicted precipitation variance ratio based on changes in mean precipitation [see Eq. (5)] and (bottom) the actual variance ratio.

Brought to you by NOAA Central Library | Unauthenticated | Downloaded 01/16/24 09:04 PM UTC

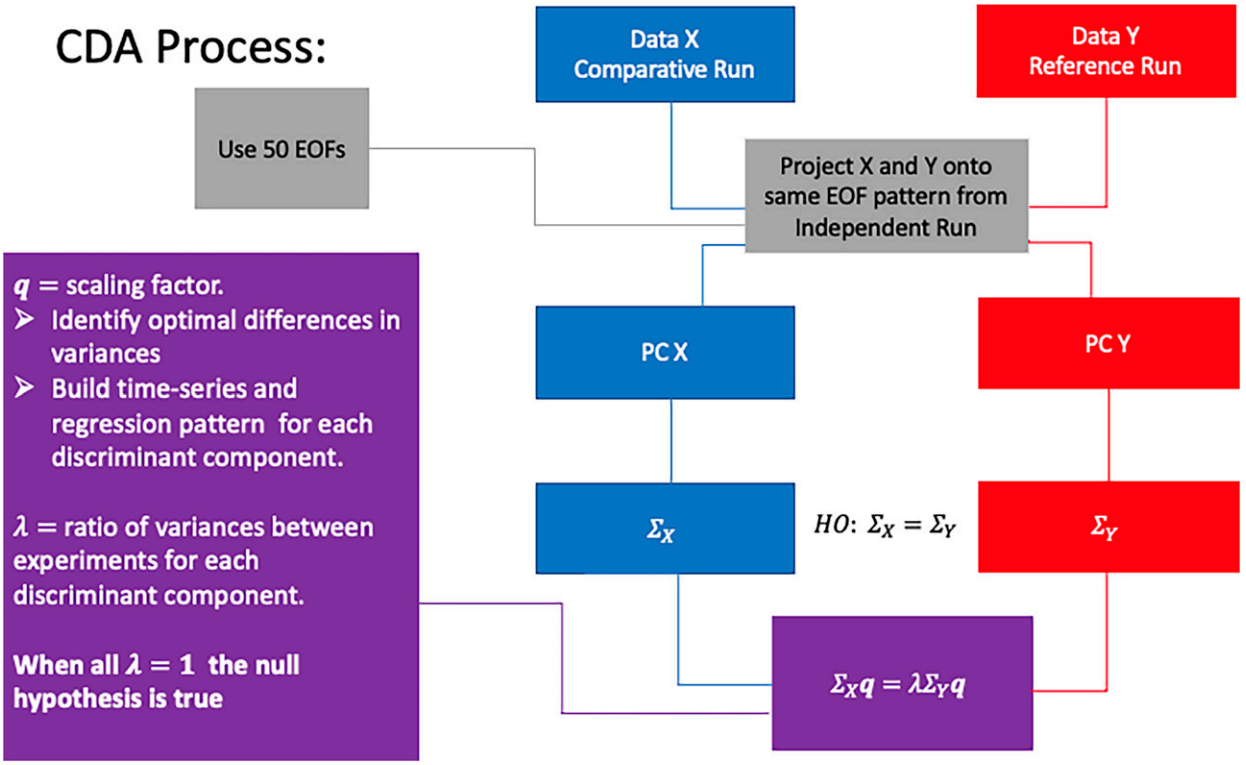

FIG. 8. Flowchart showing how CDA maximizes and minimizes the variation ratio by optimizing eigenvalues (λ) found by solving the generalized eigenvalue problem in purple.

changes in variability might not occur in the first EOF. Moreover, EOFs depend on the sample, so differences in EOFs can occur simply because of sampling variability. Since we are interested in comparing variability between a set experiments (X and Y), we want to characterize *differences* in variability. Therefore, we want to test the null hypothesis (H_0),

$$H_0 : \mathbf{\Sigma}_X = \mathbf{\Sigma}_Y, \tag{6}$$

which is tantamount to the hypothesis that the EOFs and the explained variances are the same for X and Y. Here, $\mathbf{\Sigma}_X$ is the covariance matrix of X, and $\mathbf{\Sigma}_Y$ is the covariance matrix of Y.

To quantify the differences between two covariance matrices, we find a linear combination of variables to maximize or minimize the ratio of variances. This technique is called CDA (DelSole and Tippett 2022).

Let $\mathbf{x}$ and $\mathbf{y}$ denote the variables under investigation in two experiments. At any given time, these vectors contain the values at S spatial grid points. These S values are denoted $x_1, \ldots, x_S$ and $y_1, \ldots, y_S$ and are the elements of $\mathbf{x}$ and $\mathbf{y}$, therefore,

$$\mathbf{x} = \begin{pmatrix} x_1 \\ \vdots \\ x_S \end{pmatrix} \quad \text{and} \quad \mathbf{y} = \begin{pmatrix} y_1 \\ \vdots \\ y_S \end{pmatrix}. \tag{7}$$

A linear combination of the S spatial grid points for $\mathbf{x}$ is denoted,

$$r_x = q_1 x_1 + q_2 x_2 + \cdots + q_s x_s, \tag{8}$$

where $q_1, \ldots, q_S$ are projection coefficients. Similarly, a linear combination of the Y variables is

$$r_y = q_1 y_1 + q_2 y_2 + \cdots + q_s y_s. \tag{9}$$

These linear combinations can be expressed more concisely as

$$r_x = \mathbf{q}^{\mathrm{T}}\mathbf{x} \quad \text{and} \quad r_y = \mathbf{q}^{\mathrm{T}}\mathbf{y}, \tag{10}$$

where superscript T denotes the transpose operation. To measure differences in variability, we use the ratio of variances λ, defined as

$$\lambda = \frac{\mathrm{var}[r_x]}{\mathrm{var}[r_y]} = \frac{\mathbf{q}^{\mathrm{T}}\mathbf{\Sigma}_x\mathbf{q}}{\mathbf{q}^{\mathrm{T}}\mathbf{\Sigma}_y\mathbf{q}}. \tag{11}$$

If there is no difference in covariance matrices, then λ will equal one for all choices of $\mathbf{q}$. Thus, we test whether $\lambda = 1$ for all choices of $\mathbf{q}$. We do this by finding the projection coefficients $\mathbf{q}$ that maximize or minimize λ. By maximizing or minimizing λ, we explore differences in variability (or more precisely, differences in covariance matrices) between $\mathbf{x}$ and $\mathbf{y}$.

CDA seeks to find the projection vectors that optimize λ. It is a standard result in linear algebra that the solution is

Brought to you by NOAA Central Library | Unauthenticated | Downloaded 01/16/24 09:04 PM UTC

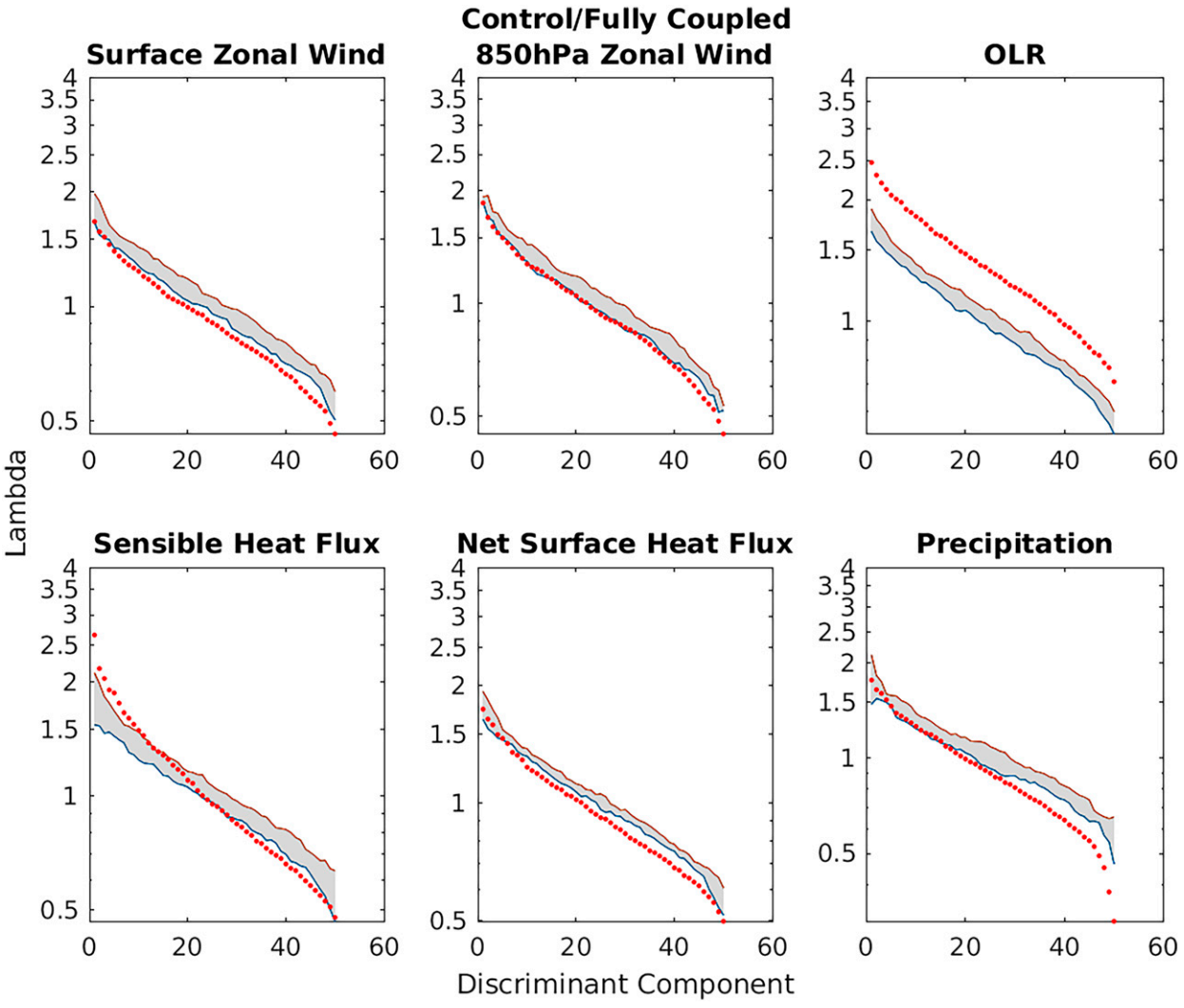

FIG. 9. Discriminant ratios for comparing precipitation, surface zonal wind, 850-hPa zonal wind, outgoing longwave radiation (olr), sensible heat flux, and net surface heat flux between the control and fully coupled runs. Red dots show the discriminant ratios, blue and brown curves show the 95% confidence interval under the null hypothesis of equal covariance matrices. The discriminant ratios were computed using 50 EOFs derived from an independent realization.

obtained by solving the generalized eigenvalue problem (Serber 2008, result 6.59),

$$\mathbf{\Sigma}_x\mathbf{q} = \lambda\mathbf{\Sigma}_y\mathbf{q}. \tag{12}$$

The eigenvalues λ are called discriminant ratios and are ordered from largest to smallest. The second eigenvalue is the largest variance ratio among components that are uncorrelated with the first and so on.

Figure 8 shows a flowchart of the CDA procedure. We use the convention that Y is the reference run and X is the run that is spun off from the reference. Thus, when comparing the fully coupled and control run, Y is the fully coupled run, and X is the control run based off of the fully coupled run. X and Y are then projected onto precomputed EOF patterns from an independent run (second ensemble member of the fully coupled run) to translate the data into principal components (PCs). Deriving EOFs from an independent run avoids overfitting the variance. We choose 50 EOFs (i.e., 50 discriminant components) based on the percent of variance explained: for all variables, the 50th EOF explains no more than 0.5% of the variance. Since a component that explains less than 0.5% of the total variance is probably not important, an analysis based on 50 EOFs is adequate. Note that using too few EOFs may fail to detect differences simply because the resulting low-dimensional space is too restrictive to capture the differences. We performed our CDA for 25, 50, and 75 EOFs, finding similar outcomes between them. Therefore, we decided to present the results for a relatively large truncation (50 EOFs) to eliminate concerns from using too few EOFs.

Our data are serially correlated, and testing significance with serially correlated data is very challenging. In this work,

Brought to you by NOAA Central Library | Unauthenticated | Downloaded 01/16/24 09:04 PM UTC

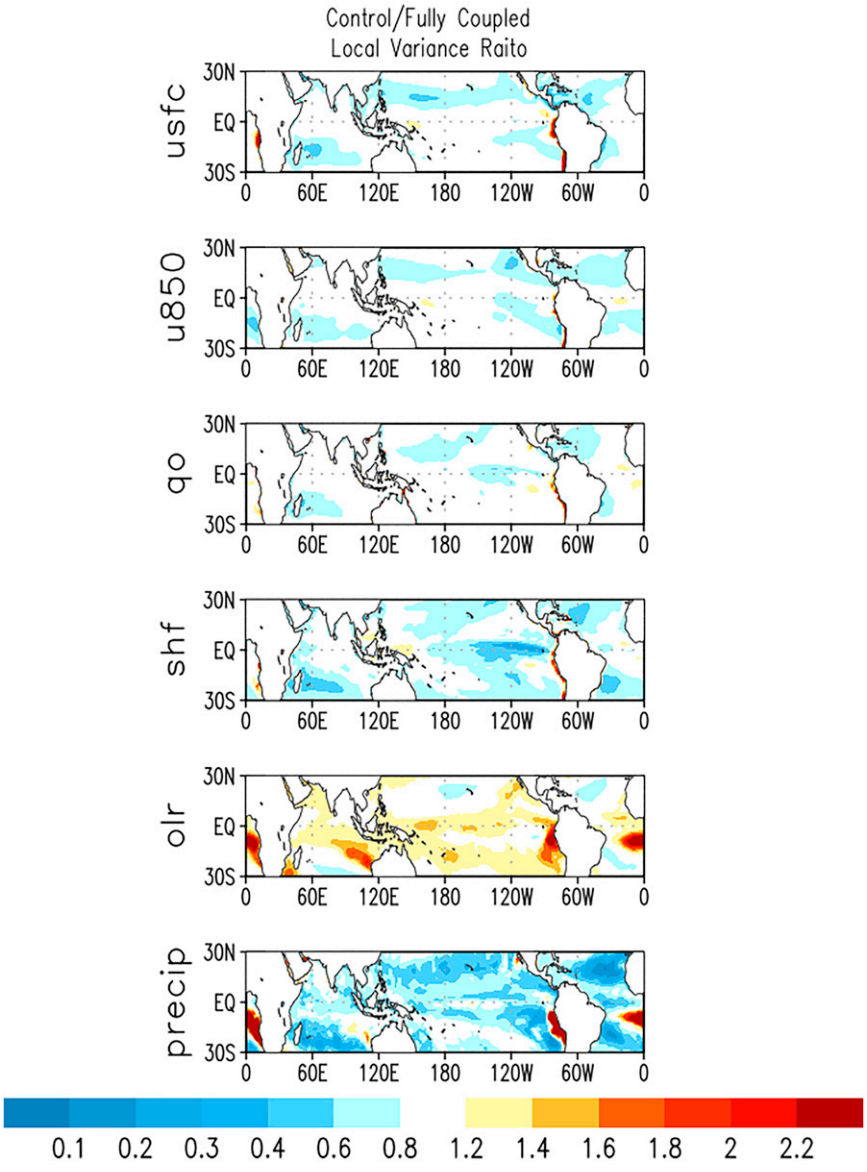

FIG. 10. Local variance ratios for precipitation (precip), surface zonal wind (usfc), 850-hPa zonal wind (u850), outgoing longwave radiation (olr), sensible heat flux (shf), and net surface heat flux (q_o) between the control and fully coupled runs.

we have chosen a simple approach that exploits the long length of the simulations. Specifically, the data are split into two halves, and then X and Y are taken from the first and second half of the same simulation. This provides a sample from the null hypothesis of no change in stochastic processes, because the time series are drawn from the same model. An advantage of this approach is that it makes no assumptions about the serial correlation of tropical variability. This procedure yields two sets of λ values, because the ratio can be formed in two ways: first over second half, or second over first half. Moreover, we applied this procedure to six other slab ocean model experiments, yielding 12 realizations of λ values. We then use the mean plus/minus two standard deviations to estimate the 95% confidence interval of λ values when the null hypothesis is true.

b. CDA results

Comparing the slab and fully coupled runs, CDA revealed that significant variance differences occurred in the precipitation, surface zonal wind, 850-hPa zonal wind, olr, sensible heat flux, and net surface heat flux (see Fig. 9).

All of the variables in Fig. 9 show more than half of their discriminant components lying outside of the confidence intervals. From this, we conclude that differences in variability cannot be expressed in a few patterns. Therefore, it is sensible

Brought to you by NOAA Central Library | Unauthenticated | Downloaded 01/16/24 09:04 PM UTC

to draw conclusions based off local changes in variance which are shown in Fig. 10. In Fig. 10 we see that the slab run has decreased variability in the precipitation, lower level zonal winds, and q_o, and increased variability in olr compared to the fully coupled run. These variance changes are a consequence of the warming pattern present in the slab run. It is important to note here that olr is an outlier for two reasons. The first is that it has no discriminate components lying inside the confidence intervals, in fact they lie distinctively higher than the other variables. This is perplexing to us, and while olr is consistent with the precipitation scaling argument discussed in section 3c, we do not have a good explanation as to why olr differs in this way. The second reason is that while the olr and precipitation variance patterns have similarities, there are still differences. This is contrary to common assumption, as olr is often a proxy for precipitation. However, olr is not precipitation, and our results suggest that olr variance is not a good proxy of precipitation variance.

We can use the results from CDA to determine if the thinning of MLD to 2 m impacts the large-scale climate on intraseasonal time scales. CDA analysis indicated that in both the 2mIOqadj and 2mIO cases, only the net surface heat flux (q_o) and latent heat flux (lhf) show a significant change in variability compared to the control run (see Fig. A2). Since the same results were obtained for 2mIO and 2mIOadj, the reduction in variance is insensitive to Q_{dp}.

Figure 11 shows the local variances of q_o for the 2mIO run. The q_o and lhf pattern from the 2mIOqadj are not shown because they have a similar pattern. The large variance decrease in q_o (and lhf) is seen just over the Indian Ocean. This is because a reduced MLD results in less thermal inertia, allowing the ocean slab to adjust quickly to atmospheric temperature changes, thereby reducing temperature differences between atmosphere and ocean, which in turn constrains the amplitude of the surface fluxes (Keerthi et al. 2016). In other words, for a given surface lhf, a thin ocean slab will change its temperature faster than a thicker slab. Since lhf acts to remove the atmosphere–ocean temperature differences, the atmosphere–ocean temperature difference is driven toward 0 more strongly in a thinner mixed layer. Therefore, since the temperature differences are smaller in the 2-m MLD cases, the variability in latent heat flux is also smaller.

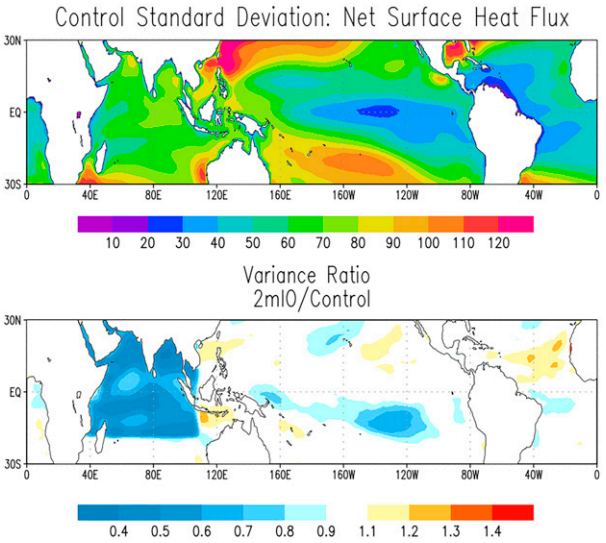

FIG. 11. (top) Local standard deviation of net surface heat flux in the control and (bottom) the variance ratio for 2mIO/control.

5. Summary and conclusions

The goal of this paper was to gain insight into the ocean's role in tropical intraseasonal variability, particularly the initiation and maintenance of the Madden–Julian oscillation. This was done by analyzing and performing a suite of sensitivity experiments with a coupled atmosphere–ocean model in which the ocean component was modified in various ways. First, the ocean was replaced by a motionless zero-dimensional slab whose heat capacity varied with longitude and latitude according to the spatially varying annually averaged mixed layer depth from the fully coupled model. To preserve the climatological surface temperature, a periodic function of time was added to the thermodynamic equation to parameterize the effect of the climatological ocean currents (known as a q-flux term). By comparing the fully coupled model with the slab model we can isolate the role of interactive ocean dynamics (e.g., ocean currents, entrainment, etc.) in atmospheric variability.

Despite precautions taken to preserve the climatology by specifying the q-flux term, the slab model has a warmer climate compared to the fully coupled model. We are able to demonstrate that this warming leads to changes in climate variability. In particular, we show that changes in precipitation that result from a warmer climate can be predicted using a scaling argument.

No significant difference in the MJO could be detected between the fully coupled and the slab version of the models. However, our modeled MJO was less persistent than the observed MJO. One major shortcoming of the models was that the mixed layer is much deeper in the Indian Ocean than in observations, particularly over the SCTR. This motivated us to investigate the impact of changing the mixed layer depth over the Indian ocean. Surprisingly, imposing varying MLDs (2, 10, 20, 30, 40, 50 m) over the Indian Ocean led to no significant change in MJO variability or persistence.

Through a statistical optimization procedure called covariance discriminant analysis, we were able to explore changes in variability on intraseasonal time scales between our model experiments in a more comprehensive fashion. Reducing the depth of the mixed layer over the Indian ocean led to a significant decrease in variability of the latent heat flux in that region, presumably because the thinner slab has a smaller heat capacity and adjusts to the atmospheric temperature more rapidly, thereby reducing the vertical temperature differences that drive the latent heat fluxes. Other than these changes, which could be explained by simple thermodynamics, no other significant changes in variability were detected in

Brought to you by NOAA Central Library | Unauthenticated | Downloaded 01/16/24 09:04 PM UTC

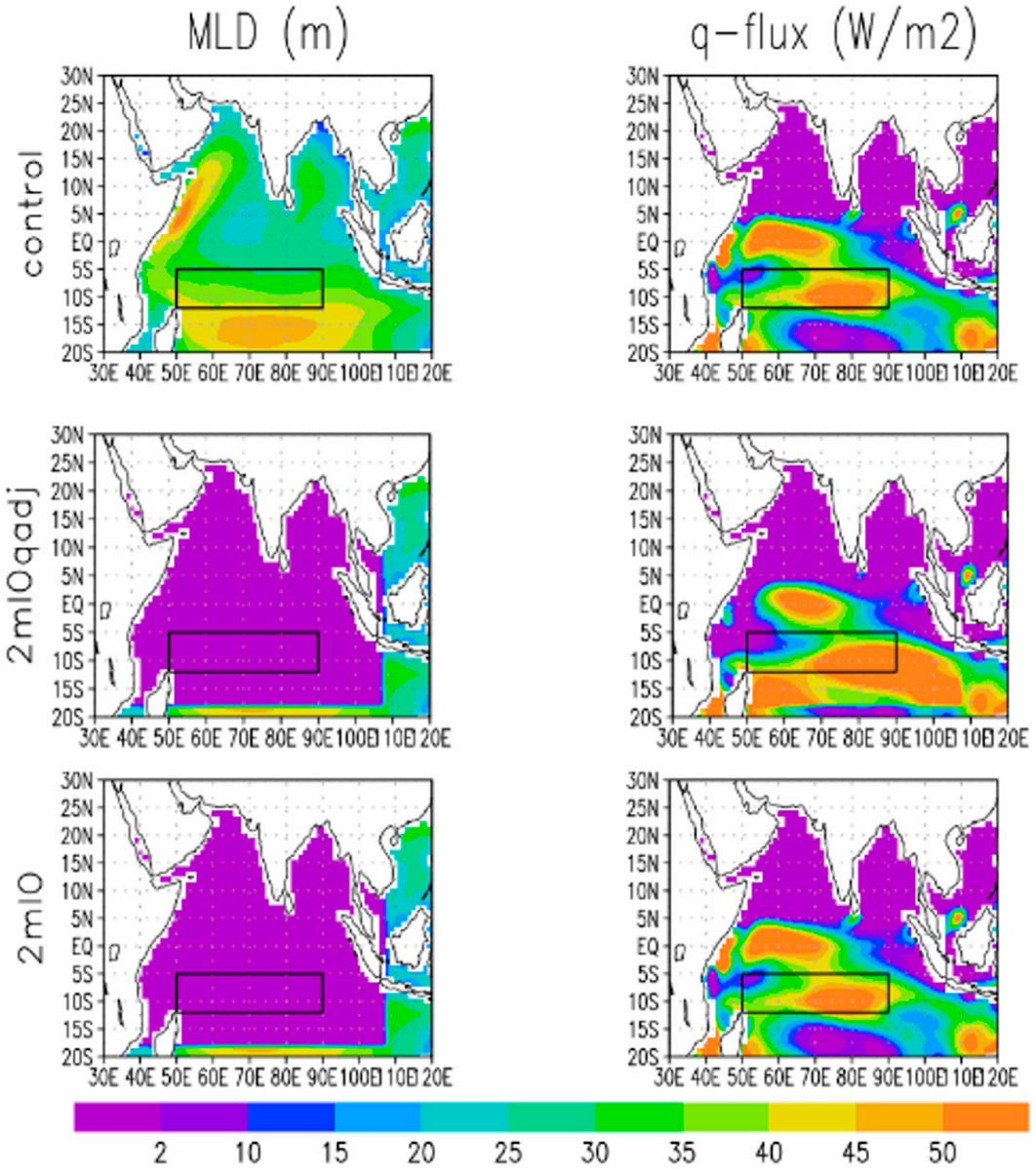

FIG. A1. Distribution of MLD and Q_{dp} for (top) control SOM run, (middle) 2mIOqadj, and (bottom) 2mIO.

response to reducing the depth of the mixed layer over the Indian ocean.

A plausible explanation for our results is that, in our particular model, the feedback between the ocean and MJO variability is weaker than in observations. Specifically, this hypothesis would explain the lack of sensitivity of MJO variability to ocean mixed layer depth, and explain the weaker persistence of MJO variability in the model than in observations. We note that previous SOM studies of this feedback are not always consistent, as some studies find a strong feedback (Maloney and Sobel 2004; Maloney and Kiehl 2002; Marshall and Plumb 2008) while others do not (e.g., Grabowski 2006) This hypothesis leads us to suggest that efforts to improve MJO variability in this model should focus on improving the feedback coupling between the MJO and the underlying ocean.

Acknowledgments. This study was supported by Mason Provost PhD Program and by NOAA's Climate Program Office's Modeling, Analysis, Predictions, and Projections program Grants NA16OAR4310146 and NA16OAR4310149.

Data availability statement. The fully coupled data are available at http://www.cesm.ucar.edu/projects/community-projects/LENS/data-sets.html. The experiment used in this project is b.e11.B20TRC5CNBDRD.f09_g16.001.cam.h1. The

Brought to you by NOAA Central Library | Unauthenticated | Downloaded 01/16/24 09:04 PM UTC

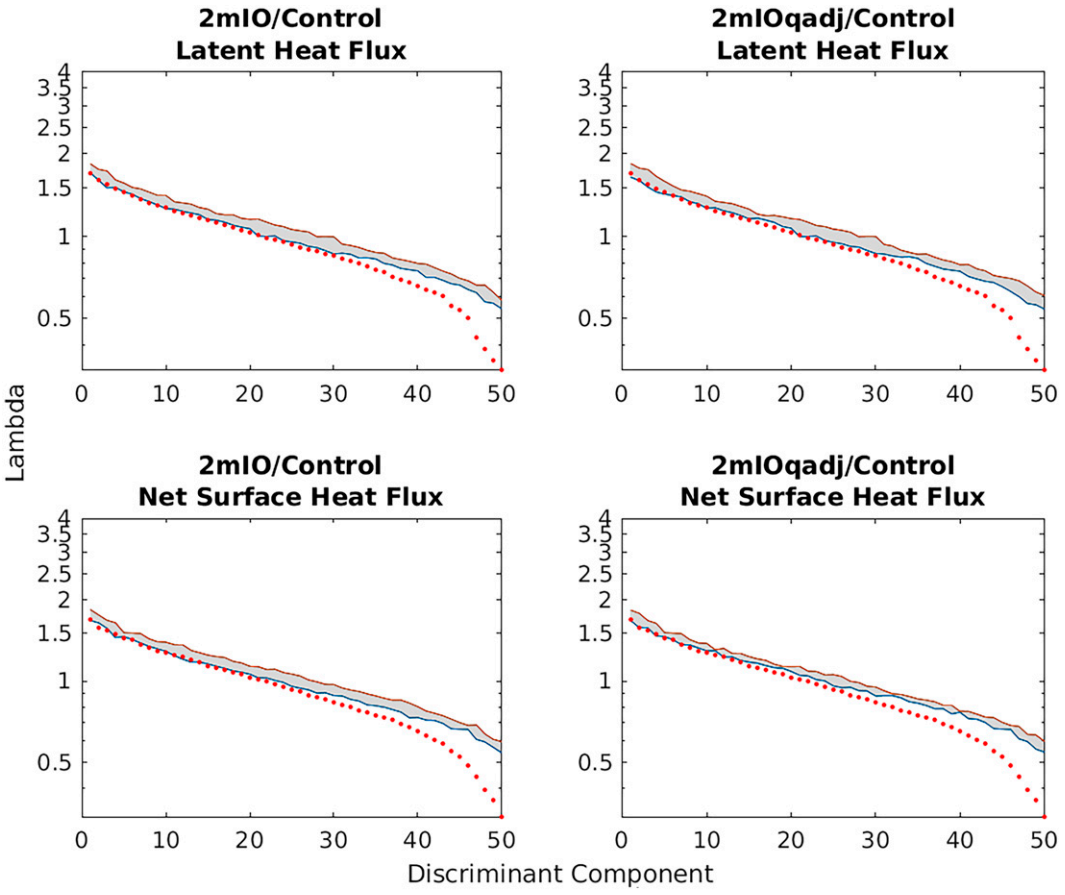

FIG. A2. Discriminant ratios for comparing latent heat flux and net surface heat flux between the 2mIO/2mIOqadj and control SOM run. Red dots show the discriminant ratios, and blue and brown curves show the 95% confidence interval under the null hypothesis of equal covariance matrices. The discriminant ratios were computed using 50 EOFs derived from an independent realization.

2mIO, 2mIOqadj, and control run data are available at ftp://cola.gmu.edu/pub/tciceron/.

APPENDIX

Additional Model Configuration Information and Results

This appendix contains two figures to further the reader's understanding of the model configuration and CDA results. Figure A1 shows the MLD and qflux spatial distribution between the control, 2mIOqadj, and 2mIO to see how these fields change under different model constraints. Figure A2 shows the corresponding discriminate ratios that are discussed but not shown in the main text.

REFERENCES

Ahn, M.-S., D. Kim, K. Sperber, I.-S. Kang, E. Maloney, D. Waliser, and H. Hendon, 2017: MJO simulation in CMIP5 climate models: MJO skill metrics and process-oriented diagnosis. *Climate Dyn.*, **49**, 4023–4045, https://doi.org/10.1007/s00382-017-3558-4.

——, and Coauthors, 2020: MJO propagation across the maritime continent: Are CMIP6 models better than CMIP5 models? *Geophys. Res. Lett.*, **47**, e2020GL087250, https://doi.org/10.1029/2020GL087250.

Anber, U., S. Wang, and A. Sobel, 2017: Coupling with ocean mixed layer leads to intraseasonal variability in tropical deep convection: Evidence from cloud-resolving simulations. *J. Adv. Model. Earth Syst.*, **9**, 616–626, https://doi.org/10.1002/2016MS000803.

Bitz, C. M., K. Shell, P. Gent, D. Bailey, G. Danabasoglu, K. Armour, M. Holland, and J. Kiehl, 2012: Climate sensitivity of the Community Climate System Model, version 4. *J. Climate*, **25**, 3053–3070, https://doi.org/10.1175/JCLI-D-11-00290.1.

Boyle, J. S., S. A. Klein, D. D. Lucas, H.-Y. Ma, J. Tannahill, and S. Xie, 2015: The parametric sensitivity of CAM5's MJO. *J. Geophys. Res. Atmos.*, **120**, 1424–1444, https://doi.org/10.1002/2014JD022507.

Bretherton, C. S., M. E. Peters, and L. E. Back, 2004: Relationships between water vapor path and precipitation over the tropical oceans. *J. Climate*, **17**, 1517–1528, https://doi.org/10.1175/1520-0442(2004)017<1517:RBWVPA>2.0.CO;2.

Bui, H. X., and E. D. Maloney, 2019: Transient response of MJO precipitation and circulation to greenhouse gas forcing.

Brought to you by NOAA Central Library | Unauthenticated | Downloaded 01/16/24 09:04 PM UTC

Geophys. Res. Lett., **46**, 13 546–13 555, https://doi.org/10.1029/2019GL085328.

Bulusu, S., 2016: Poster: The role of ocean dynamics in the MJO initiation over the Indian Ocean. Department of Atmospheric and Oceanic Sciences Colloquium Series, University of South Carolina, https://www.aos.wisc.edu/posters/2016-17/Subra_Bulusu.jpg.

Cavanaugh, N. R., A. Gershunov, A. K. Panorska, and T. J. Kozubowski, 2015: The probability distribution of intense daily precipitation. *Geophys. Res. Lett.*, **42**, 1560–1567, https://doi.org/10.1002/2015GL063238.

Conley, A. J., 2012: Description of the NCAR Community Atmosphere Model (CAM 5.0). NCAR Tech. Note NCAR/TN-486+STR, 289 pp., https://www2.cesm.ucar.edu/models/cesm1.0/cam/docs/description/cam5_desc.pdf.

Dasgupta, P., A. Metya, C. V. Naidu, M. Singh, and M. K. Roxy, 2020: Exploring the long-term changes in the Madden Julian Oscillation using machine learning. *Sci. Rep.*, **10**, 18567, https://doi.org/10.1038/s41598-020-75508-5.

de Boyer Montégut, C., G. Madec, A. S. Fischer, A. Lazar, and D. Iudicone, 2004: Mixed layer depth over the global ocean: An examination of profile data and a profile-based climatology. *J. Geophys. Res.*, **109**, C12003, https://doi.org/10.1029/2004JC002378.

DelSole, T., and M. Tippett, 2022: Covariance discriminant analysis. *Statistical Methods for Climate Scientists*, Cambridge University Press, 366–398, https://doi.org/10.1017/9781108659055.017.

DeMott, C. A., N. P. Klingaman, and S. J. Woolnough, 2015: Atmosphere-ocean coupled processes in the Madden-Julian oscillation. *Rev. Geophys.*, **53**, 1099–1154, https://doi.org/10.1002/2014RG000478.

——, ——, W.-L. Tseng, M. A. Burt, Y. Gao, and D. A. Randall, 2019: The convection connection: How ocean feedbacks affect tropical mean moisture and MJO propagation. *J. Geophys. Res. Atmos.*, **124**, 11 910–11 931, https://doi.org/10.1029/2019JD031015.

Drushka, K., J. Sprintall, S. Gille, and S. Wijffels, 2012: In situ observations of Madden–Julian oscillation mixed layer dynamics in the Indian and western Pacific Oceans. *J. Climate*, **25**, 2306–2328, https://doi.org/10.1175/JCLI-D-11-00203.1.

Duvel, J. P., R. Roca, and J. Vialard, 2004: Ocean mixed layer temperature variations induced by intraseasonal convective perturbations over the Indian Ocean. *J. Atmos. Sci.*, **61**, 1004–1023, https://doi.org/10.1175/1520-0469(2004)061<1004:OMLTVI>2.0.CO;2.

Flatau, M., P. J. Flatau, P. Phoebus, and P. P. Niiler, 1997: The feedback between equatorial convection and local radiative and evaporative processes: The implications for intraseasonal oscillations. *J. Atmos. Sci.*, **54**, 2373–2386, https://doi.org/10.1175/1520-0469(1997)054<2373:TFBECA>2.0.CO;2.

Goswami, B. N., R. S. Ajayamohan, P. K. Xavier, and D. Sengupta, 2003: Clustering of synoptic activity by Indian summer monsoon intraseasonal oscillations. *Geophys. Res. Lett.*, **30**, 1431, https://doi.org/10.1029/2002GL016734.

Gottschalck, J., and Coauthors, 2010: A framework for assessing operational Madden–Julian oscillation forecasts: A CLIVAR MJO working group project. *Bull. Amer. Meteor. Soc.*, **91**, 1247–1258, https://doi.org/10.1175/2010BAMS2816.1.

Grabowski, W. W., 2006: Impact of explicit atmosphere–ocean coupling on MJO-like coherent structures in idealized aquaplanet simulations. *J. Atmos. Sci.*, **63**, 2289–2306, https://doi.org/10.1175/JAS3740.1.

Hagos, S., and Coauthors, 2020: Atmospheric convection and air–sea interactions over the tropical oceans: Scientific progress, challenges, and opportunities. *Bull. Amer. Meteor. Soc.*, **101**, E253–E258, https://doi.org/10.1175/BAMS-D-19-0261.1.

Held, I. M., and B. J. Soden, 2006: Robust responses of the hydrological cycle to global warming. *J. Climate*, **19**, 5686–5699, https://doi.org/10.1175/JCLI3990.1.

Hermes, J. C., and C. Reason, 2008: Annual cycle of the South Indian Ocean (Seychelles-Chagos) thermocline ridge in a regional ocean model. *J. Geophys. Res.*, **113**, C04035, https://doi.org/10.1029/2007JC004363.

——, and C. J. C. Reason, 2009: The sensitivity of the Seychelles–Chagos thermocline ridge to large-scale wind anomalies. *ICES J. Mar. Sci.*, **66**, 1455–1466, https://doi.org/10.1093/icesjms/fsp074.

Huang, C. J., F. Qiao, and D. Dai, 2014: Evaluating CMIP5 simulations of mixed layer depth during summer. *J. Geophys. Res. Oceans*, **119**, 2568–2582, https://doi.org/10.1002/2013JC009535.

Hung, M.-P., J.-L. Lin, W. Wang, D. Kim, T. Shinoda, and S. Weaver, 2013: MJO and convectively coupled equatorial waves simulated by CMIP5 climate models. *J. Climate*, **26**, 6185–6214, https://doi.org/10.1175/JCLI-D-12-00541.1.

Hurrell, J. W., and Coauthors, 2013: The Community Earth System Model: A framework for collaborative research. *Bull. Amer. Meteor. Soc.*, **94**, 1339–1360, https://doi.org/10.1175/BAMS-D-12-00121.1.

Hwang, Y. T., and D. M. Frierson, 2013: Link between the double-Intertropical Convergence Zone problem and cloud biases over the Southern Ocean. *Proc. Natl. Acad. Sci. USA*, **110**, 4935–4940, https://doi.org/10.1073/pnas.1213302110.

Inness, P. M., and J. M. Slingo, 2003: Simulation of the Madden–Julian oscillation in a coupled general circulation model. Part I: Comparison with observations and an atmosphere-only GCM. *J. Climate*, **16**, 345–364, https://doi.org/10.1175/1520-0442(2003)016<0345:SOTMJO>2.0.CO;2.

Jiang, X., and Coauthors, 2015: Vertical structure and physical processes of the Madden-Julian oscillation: Exploring key model physics in climate simulations. *J. Geophys. Res. Atmos.*, **120**, 4718–4748, https://doi.org/10.1002/2014JD022375.

——, A. F. Adames, M. Zhao, D. Waliser, and E. Maloney, 2018: A unified moisture mode framework for seasonality of the Madden–Julian oscillation. *J. Climate*, **31**, 4215–4224, https://doi.org/10.1175/JCLI-D-17-0671.1.

——, and Coauthors, 2020: Fifty years of research on the Madden-Julian oscillation: Recent progress, challenges, and perspectives. *J. Geophys. Res. Atmos.*, **125**, e2019JD030911, https://doi.org/10.1029/2019JD030911.

Kalnay, E., and Coauthors, 1996: The NCEP/NCAR 40-Year Reanalysis Project. *Bull. Amer. Meteor. Soc.*, **77**, 437–471, https://doi.org/10.1175/1520-0477(1996)077<0437:TNYRP>2.0.CO;2.

Kay, J. E., and Coauthors, 2015: The Community Earth System Model (CESM) large ensemble project: A community resource for studying climate change in the presence of internal climate variability. *Bull. Amer. Meteor. Soc.*, **96**, 1333–1349, https://doi.org/10.1175/BAMS-D-13-00255.1.

Keerthi, M., M. Lengaigne, K. Drushka, J. Vialard, C. de Boyer Montegut, S. Pous, M. Levy, and P. M. Muraleedharan, 2016: Intraseasonal variability of mixed layer depth in the tropical Indian Ocean. *Climate Dyn.*, **46**, 2633–2655, https://doi.org/10.1007/s00382-015-2721-z.

Kim, D., and Coauthors, 2009: Application of MJO simulation diagnostics to climate models. *J. Climate*, **22**, 6413–6436, https://doi.org/10.1175/2009JCLI3063.1.

Brought to you by NOAA Central Library | Unauthenticated | Downloaded 01/16/24 09:04 PM UTC

Kirtman, B., and Coauthors, 2014: The North American Multimodel Ensemble: Phase-1 seasonal-to-interannual prediction; Phase-2 toward developing intraseasonal prediction. *Bull. Amer. Meteor. Soc.*, **95**, 585–601, https://doi.org/10.1175/BAMS-D-12-00050.1.

Klotzbach, P. J., 2010: On the Madden–Julian oscillation–Atlantic hurricane relationship. *J. Climate*, **23**, 282–293, https://doi.org/10.1175/2009JCLI2978.1.

Lan, Y.-Y., H.-H. Hsu, W.-L. Tseng, and L.-C. Jiang, 2022: Embedding a one-column ocean model in the Community Atmosphere Model 5.3 to improve Madden–Julian Oscillation simulation in boreal winter. *Geosci. Model Dev.*, **15**, 5689–5712, https://doi.org/10.5194/gmd-15-5689-2022.

Lau, W. K.-M., and D. E. Waliser, 2012: *Intraseasonal Variability in the Atmosphere-Ocean Climate System*. 2nd ed. Springer, 613 pp.

Liebmann, B., and C. A. Smith, 1996: Description of a complete (interpolated) outgoing longwave radiation datase. *Bull. Amer. Meteor. Soc.*, **77**, 1275–1277, https://doi.org/10.1175/1520-0477-77.6.1274.

Lin, J.-L., and Coauthors, 2006: Tropical intraseasonal variability in 14 IPCC AR4 climate models. Part I: Convective signals. *J. Climate*, **19**, 2665–2690, https://doi.org/10.1175/JCLI3735.1.

Ling, J., and Coauthors, 2017: Challenges and opportunities in MJO studies. *Bull. Amer. Meteor. Soc.*, **98**, ES53–ES56, https://doi.org/10.1175/BAMS-D-16-0283.1.

Liu, P., Q. Zhang, C. Zhang, Y. Zhu, M. Khairoutdinov, H. Kim, C. Schumacher, and M. Zhang, 2016: A revised real-time multivariate MJO index. *Mon. Wea. Rev.*, **144**, 627–642, https://doi.org/10.1175/MWR-D-15-0237.1.

Madden, R. A., and P. R. Julian, 1971: Detection of a 40–50 day oscillation in the zonal wind in the tropical Pacific. *J. Atmos. Sci.*, **28**, 702–708, https://doi.org/10.1175/1520-0469(1971)028<0702:DOADOI>2.0.CO;2.

——, and ——, 1972: Description of global-scale circulation cells in the tropics with a 40–50 day period. *J. Atmos. Sci.*, **29**, 1109–1123, https://doi.org/10.1175/1520-0469(1972)029<1109:DOGSCC>2.0.CO;2.

Maloney, E. D., and J. T. Kiehl, 2002: Intraseasonal eastern Pacific precipitation and SST variations in a GCM coupled to a slab ocean model. *J. Climate*, **15**, 2989–3007, https://doi.org/10.1175/1520-0442(2002)015<2989:IEPPAS>2.0.CO;2.

——, and A. Sobel, 2004: Surface fluxes and ocean coupling in the tropical intraseasonal oscillation. *J. Climate*, **17**, 4368–4386, https://doi.org/10.1175/JCLI-3212.1.

Marshall, A. G., O. Alves, and H. H. Hendon, 2008: An enhanced moisture convergence–evaporation feedback mechanism for MJO air–sea interaction. *J. Atmos. Sci.*, **65**, 970–986, https://doi.org/10.1175/2007JAS2313.1.

Marshall, J., and R. A. Plumb, 2008: *Atmosphere, Ocean, and Climate Dynamics. An Introductory Text*. International Geophysics Series, Vol. 93, Academic Press, 319 pp.

Martin, Z., F. Vitart, S. Wang, and A. Sobel, 2020: The impact of the stratosphere on the MJO in a forecast model. *J. Geophys. Res. Atmos.*, **125**, e2019JD032106, https://doi.org/10.1029/2019JD032106.

Masumoto, Y., and G. Meyers, 1998: Forced Rossby waves in the southern tropical Indian Ocean. *J. Geophys. Res.*, **103**, 27 589–27 602, https://doi.org/10.1029/98JC02546.

McCreary, J. P., P. K. Kundu, and R. L. Molinari, 1993: A numerical investigation of dynamics, thermodynamics, and mixed-layer processes in the Indian Ocean. *Prog. Oceanogr.*, **31**, 181–244, https://doi.org/10.1016/0079-6611(93)90002-U.

NCEP, NWS, NOAA, and U. DoC, 1994: NCEP/NCAR global reanalysis products, 1948-continuing, updated monthly. NOAA/PSL Research Data Archive, accessed 16 March 2020, https://doi.org/10.5065/KHX2-FJ42.

Olsson, J., and P. Burlando, 2002: Reproduction of temporal scaling by a rectangular pulses rainfall model. *Hydrol. Processes*, **16**, 611–630, https://doi.org/10.1002/hyp.307.

Phillips, H., and Coauthors, 2021: Progress in understanding of Indian Ocean circulation, variability, air-sea exchange and impacts on biogeochemistry. *Ocean Sci.*, **17**, 1677–1751, https://doi.org/10.5194/os-17-1677-2021.

Ray, P., and C. Zhang, 2010: A case study of the mechanics of extratropical influence on the initiation of the Madden-Julian oscillation. *J. Atmos. Sci.*, **67**, 515–528, https://doi.org/10.1175/2009JAS3059.1.

Serber, G., 2008: *A Matrix Handbook for Statisticians*. John Wiley and Sons, Ltd., 592 pp.

Shin, S. S., S. D. Park, and B. K. Choi, 2016: Universal power law for relationship between rainfall kinetic energy and rainfall intensity. *Adv. Meteor.*, **2016**, 2494681, https://doi.org/10.1155/2016/2494681.

Shinoda, T., W. Han, L. Zamudio, R.-C. Lien, and M. Katsumata, 2017: Remote ocean response to the Madden–Julian oscillation during the DYNAMO field campaign: Impact on Somali current system and the Seychelles–Chagos thermocline ridge. *Atmosphere*, **8**, 171, https://doi.org/10.3390/atmos8090171.

Shoup, C. G., H. L. Roman-Stork, and B. Subrahmanyam, 2020: Analysis of coupled oceanic and atmospheric preconditioning for primary Madden-Julian oscillation events across ENSO phases. *J. Geophys. Res. Oceans*, **125**, e2020JC016358, https://doi.org/10.1029/2020JC016358.

Song, X., and G. J. Zhang, 2018: The roles of convection parameterization in the formation of double ITCZ syndrome in the NCAR CESM: I. Atmospheric processes. *J. Adv. Model. Earth Syst.*, **10**, 842–866, https://doi.org/10.1002/2017MS001191.

Taraphdar, S., F. Zhang, L. R. Leung, X. Chen, and O. M. Pauluis, 2018: MJO affects the monsoon onset timing over the Indian region. *Geophys. Res. Lett.*, **45**, 10 011–10 018, https://doi.org/10.1029/2018GL078804.

Trenary, L. L., and W. Han, 2012: Intraseasonal-to-interannual variability of South Indian Ocean sea level and thermocline: Remote versus local forcing. *J. Phys. Oceanogr.*, **42**, 602–627, https://doi.org/10.1175/JPO-D-11-084.1.

Vialard, J., G. R. Foltz, M. J. McPhaden, J. P. Duvel, and C. de Boyer Montégut, 2008: Strong Indian Ocean sea surface temperature signals associated with the Madden–Julian oscillation in late 2007 and early 2008. *Geophys. Res. Lett.*, **35**, L19608, https://doi.org/10.1029/2008GL035238.

——, and Coauthors, 2009: Supplement to cirene: Air—Sea interactions in the Seychelles—Chagos thermocline ridge region. *Bull. Amer. Meteor. Soc.*, **90**, ES1–ES4, https://doi.org/10.1175/2008BAMS2499.2.

Waliser, D., and Coauthors, 2009: MJO simulation diagnostics. *J. Climate*, **22**, 3006–3030, https://doi.org/10.1175/2008JCLI2731.1.

Wang, B., 2006: *The Asian Monsoon*. Springer and Praxis Publishing, 787 pp.

——, and X. Xie, 1998: Coupled modes of the warm pool climate system. Part I: The role of air-sea interaction in maintaining Madden–Julian oscillation. *J. Climate*, **11**, 2116–2135, https://doi.org/10.1175/1520-0442-11.8.2116.

Wang, L., K. Kodera, and W. Chen, 2012: Observed triggering of tropical convection by a cold surge: Implications for MJO

Brought to you by NOAA Central Library | Unauthenticated | Downloaded 01/16/24 09:04 PM UTC

initiation. *Quart. J. Roy. Meteor. Soc.*, **138**, 1740–1750, https://doi.org/10.1002/qj.1905.

Wang, W., A. Kumar, J. Xiouhua Fu, and M.-P. Hung, 2015: What is the role of the sea surface temperature uncertainty in the prediction of tropical convection associated with the MJO? *Mon. Wea. Rev.*, **143**, 3156–3175, https://doi.org/10.1175/MWR-D-14-00385.1.

Wheeler, M. C., and H. H. Hendon, 2004: An all-season real-time multivariate MJO index: Development of an index for monitoring and prediction. *Mon. Wea. Rev.*, **132**, 1917–1932, https://doi.org/10.1175/1520-0493(2004)132<1917:AARMMI>2.0.CO;2.

Woodberry, K. E., M. Luther, and J. J. O'Brien, 1989: The wind-driven seasonal circulation in the southern tropical Indian Ocean. *J. Geophys. Res.*, **94**, 17 985–18 002, https://doi.org/10.1029/JC094iC12p17985.

Woolnough, S. J., J. M. Slingo, and B. J. Hoskins, 2000: The relationship between convection and sea surface temperature on intraseasonal timescales. *J. Climate*, **13**, 2086–2104, https://doi.org/10.1175/1520-0442(2000)013<2086:TRBCAS>2.0.CO;2.

Xie, S.-P., H. Annamalai, F. A. Schott, and J. P. McCreary, 2002: Structure and mechanisms of south Indian Ocean climate variability. *J. Climate*, **15**, 864–878, https://doi.org/10.1175/1520-0442(2002)015<0864:SAMOSI>2.0.CO;2.

Zhang, C., 2013: Madden–Julian oscillation: Bridging weather and climate. *Bull. Amer. Meteor. Soc.*, **94**, 1849–1870, https://doi.org/10.1175/BAMS-D-12-00026.1.

Zhang, G., and N. A. McFarlane, 1995: Sensitivity of climate simulations to the parameterization of cumulus convection in the Canadian Climate Centre general circulation model. *Atmos.–Ocean*, **33**, 407–446, https://doi.org/10.1080/07055900.1995.9649539.

Brought to you by NOAA Central Library | Unauthenticated | Downloaded 01/16/24 09:04 PM UTC